Batteries

A CaI₂-Based Electrolyte Enabled by Borate Ester Anion Receptors for Reversible Ca–Organic and Ca–Se Batteries

Zhen Hou+, Rui Zhou+, Kai Liu, Junwu Zhu,* and Biao Zhang*

Abstract: Passivating solid electrolyte interphases (SEIs) in Ca metal anodes constitute a long-standing challenge, as they block Ca^{2+} transport and inhibit reversible Ca deposition/stripping. Current solutions focus primarily on boron/aluminum-based electrolytes to mitigate such interfacial issues by producing Ca^{2+}-conductive species, yet the complex synthetic procedure of these salts restricts the widespread application. Moreover, whether any inorganic phases possess decent Ca^{2+} conductivity within SEIs remains ambiguous. Herein, we report that a commercially available CaI₂-dimethoxyethane electrolyte supports reversible Ca/Ca^{2+} redox reactions via forming CaI₂-involved SEI, inspired by our density functional theory calculations where CaI₂ species is predicted to possess the lowest Ca^{2+} diffusion barrier among a range of inorganic phases. We further materialize this finding by introducing a serial of borate ester anion receptors, resulting in the formation of CaI₂/borides hybrid SEIs with an enhanced Ca^{2+} conductivity. Consequently, the resultant electrolytes realize a 7-fold reduction in deposition/stripping overpotential compared to anion receptor-free one, allowing for the construction of reversible Ca-metal full cells with high-capacity selenium and organic cathodes.

Introduction

Multivalent batteries have attracted increasing attention due to their multi-electron reactions during the insertion/extraction of each charge carrier, bringing the hope of breaking the energy density limit of current battery systems.[1] In particular, Ca metal batteries are prized for the delightful electrochemical characteristics of Ca anodes, such as a low redox potential of −2.87 V vs. standard hydrogen electrode and high theoretical volumetric capacity of 2073 mAh cm⁻³.[2] Besides, Ca element is abundant in Earth's crust (ranking fifth), benefiting the deployment of large-scale Ca metal-based storage systems. However, Ca/Ca^{2+} redox reactions are nearly inactive in most conventional nonaqueous electrolytes owing to the formation of ionic insulating solid electrolyte interphases (SEIs) on Ca metal anodes.[3] For

instance, Ca deposition/stripping was irreversible in calcium perchlorate Ca(ClO₄)₂-propylene carbonate (PC) electrolyte because of the formed passivating Ca(OH)₂/CaCO₃ containing SEI.[4] This long-standing challenge hinders the advancement of rechargeable Ca metal batteries.

To achieve reversible Ca systems, extensive investigations have been conducted to construct ionic conductive SEIs through screening electrolyte recipes.[5] In 2016, Ponrouch et al. constituted the first step in enabling feasible Ca deposition/stripping under calcium tetrafluoroborate Ca(BF₄)₂-ethylene carbonate (EC)/PC electrolyte, despite an operation temperature of over 75 °C.[6] Noteworthily, replacing Ca(BF₄)₂ with calcium bis(trifluoromethanesulfonyl)imide Ca(TFSI)₂, led to an irreversible Ca metal anode. The favorable role of Ca(BF₄)₂-derived SEI was attributed to the presence of cross-linked boron polymer for transferring Ca^{2+}.[7] A few feasible boron center-based electrolytes have been subsequently proposed to induce the ionic-conductive components in SEIs. Bruce's group developed a calcium borohydride Ca(BH₄)₂-tetrahydrofuran (THF) electrolyte, allowing for the operation of Ca metal anodes under room temperature.[8] However, because of the highly reducing feature of BH_4^- anion, Ca(BH₄)₂ electrolytes naturally suffer from low oxidation stability.[9] To address this dilemma, several researchers synthesized calcium tetrakis(hexafluoroisopropyloxy)borate Ca[B(hfip)₄]₂ and calcium monocarborane Ca(CB₁₁H₁₂)₂ salts, bringing about a high anodic stability of over 4.0 V vs. Ca/Ca^{2+}.[10] Considering the chemical similarity between B and Al elements, Al-based calcium fluorinated alkoxyaluminate Ca[Al(hfip)₄]₂[11] and calcium tetrakis(perfluoro-tert-butoxy) aluminate Ca(TPFA)₂[12] salts have also been synthesized for reversible Ca metal anodes.

Despite these exciting progresses, several questions regarding electrolyte and SEI design remain unresolved. On

[*] Prof. Z. Hou,+ Dr. R. Zhou,+ Prof. B. Zhang
Department of Applied Physics
The Hong Kong Polytechnic University
Hong Kong 999077, China
E-mail: biao.ap.zhang@polyu.edu.hk

Prof. Z. Hou,+ K. Liu, Prof. J. Zhu
Key Laboratory for Soft Chemistry and Functional Materials of Ministry of Education, School of Chemistry and Chemical Engineering
Nanjing University of Science and Technology
Nanjing 210094, China
E-mail: zhujw@njust.edu.cn

[+] These authors contributed equally to this work.

the one hand, current boron/aluminum-based Ca electrolytes either exhibit insufficient oxidation stability or require a rigorous synthetic procedure. This underscores the need for a readily available electrolyte system suitable for constructing reversible calcium metal batteries (e.g., high-capacity Ca-selenium full cells). On the other hand, most inorganic phases, such as CaF_2, $CaCO_3$ and CaO, as Ca^{2+} insulators nearly hinder Ca^{2+} transfer within SEIs. It is still unclear whether any inorganic species support Ca^{2+} diffusion, leading to ambiguity in SEI design.[7] This necessitates the exploration of beneficial inorganic Ca^{2+} conducting candidates. The lesson from the analogous divalent Mg battery system suggests the opportunities in halide-derived salts, as inspired by the success of $MgCl_2$ in promoting Mg reversibility.[13] Herein, we demonstrate that a readily available CaI_2-dimethoxyethane electrolyte enables reversible Ca deposition/stripping. It is attributed to the formation of unique SEI containing the ionic conductive CaI_2 species, which possesses a significantly lower Ca^{2+} migration barrier than other calcium halides. Furthermore, we introduce a collection of borate ester anion receptors to enhance CaI_2 dissociation by leveraging B–I Lewis acid-base reactions, leading to an order of magnitude enhancement in Ca^{2+} diffusion in bulk electrolytes and within SEIs. These improvements primarily originate from the promoted salt dissociation degree and the formed CaI_2/borides hybrid SEIs with an increased Ca^{2+} conductivity. Consequently, Ca deposition/stripping overpotential is reduced by a factor of seven in the presence of anion receptors, enabling the reversible operation of Ca|3,4,9,10-perylenetetracarboxylic (PTCDI) and Ca-selenium (Se) full cells. These findings offer fresh insight into Ca electrolyte development and prove the inorganic phases of SEI could also advance the Ca^{2+} diffusion.

Results and Discussion

Reversible Ca Metal Anodes in CaI₂-Based Electrolytes

To examine the capability of potential ion-conductive SEI components, we compute the Ca^{2+} diffusion barriers in relevant calcium halide phases (i.e., CaF_2, $CaCl_2$, $CaBr_2$, and CaI_2) using density functional theory (DFT) (Figure 1a and Figure S1). Among them, the CaF_2 phase possesses the largest barrier of 2.8 eV, indicating its Ca^{2+}-insulating nature, in consistency with previous reports.[7] $CaCl_2$ and $CaBr_2$ exhibit much lower diffusion barriers compared with CaF_2. But still, the values are relatively large (>1.5 eV), insufficient for bulk Ca^{2+} conduction. Interestingly, CaI_2 has a surprisingly low Ca^{2+} diffusion barrier of 0.4 eV (Figure 1b). Such a value is very close to those fast lithium-ion conductors and suggests potential bulk Ca^{2+} transport within the CaI_2 component in SEI. After careful examination, CaI_2 possesses interconnected ion diffusion channels evenly distributed in a layered manner, sharing resemblance of known layered lithium-ion cathode materials like $LiCoO_2$. More importantly, the I^- anion framework is characterized by a softer lattice compared to other calcium halides, further

supporting the fast ion transport. Additionally, Ca^{2+} diffusion barriers of inorganic species (i.e., $CaCO_3$, CaO, Ca-$(OH)_2$, and CaH_2) present in the previous reports' SEIs are calculated for comparison with CaI_2. These phases have much higher diffusion barriers (Figure S1), further implying the superiority of CaI_2 in transferring Ca^{2+} over classic inorganic components in SEIs.

To verify this conjecture, we dissolve calcium halide salts into dimethoxyethane (G1) solvents that are widely used in the Ca system, and examine their compatibility with Ca metal anodes. CaI_2 can be dissolved into G1 solvent (hereafter represented as CaI_2-G1 electrolyte), despite a low saturated concentration of ~0.015 M. By sharp contrast, CaF_2, $CaCl_2$ and $CaBr_2$ salts are almost insoluble in G1 solvent owing to their smaller anion sizes with a more intensive charge density than I^-, leading to a stronger interaction with Ca^{2+}. Therefore, the $Ca(TFSI)_2$ salt, which produces CaF_2-rich interfaces,[7] is utilized to explore the effect of CaF_2 and serve as the control group (denoted as $Ca(TFSI)_2$-G1 electrolyte). Because of the low concentration of 0.015 M, both CaI_2-G1 and $Ca(TFSI)_2$-G1 electrolytes display a low ionic conductivity of several $\mu S\,cm^{-1}$. The latter owns a larger ionic conductivity (Figure S2), stemming from a higher dissociation degree of large $TFSI^-$ anion compared to I^- one.[14] It is worth noting that such a conductivity could still support the reversible Ca deposition/stripping process provided an optimal interphase is built, evidenced by the case of Mg anodes in the electrolytes with similar conductivity values.[15] Ca|Ca symmetric cells are assembled with these two electrolytes to correlate with Ca reversibility. As shown in Figure 1c, Ca deposition/stripping potentials dramatically increase to 5 V in $Ca(TFSI)_2$-G1 electrolytes at $0.02\,mA\,cm^{-2}$, indicating the poor reversibility of Ca metal anodes. By contrast, the CaI_2 counterpart enables feasible Ca deposition/stripping, despite a slightly large polarization voltage of ~0.7 V.

Electrochemical impedance spectroscopy (EIS), a powerful tool to reflect reaction kinetics of diverse electrochemical steps, is performed using cycled Ca|Ca cells in CaI_2-G1 and $Ca(TFSI)_2$-G1 electrolytes to understand the underlying reasons for their different Ca reversibility. It is observed that the significantly enhanced Ca^{2+} diffusion within SEI is mainly responsible for the improved reaction kinetics in the CaI_2-G1 electrolyte, ascribed to the presence of ionic conductive CaI_2 species in its SEI (see Figure S3 and S4 for details). Note that the formation of salt-participated SEIs does not come as a surprise, which has been reported in the systems where the anions of electrolyte salts are present in their lowest valence state.[16] The polymer matrix aids in preventing the dissolution of CaI_2 species into the electrolytes, allowing them to be stably presented in SEIs.

Although CaI_2-G1 electrolyte enables reversible Ca deposition/stripping, a relatively large overpotential is still observed, primarily attributed to a low CaI_2 salt solubility. Theoretically, raising CaI_2 salt concentration can bring about more Ca^{2+} charge carriers in electrolytes for higher ionic conductivity and more ionic conductive CaI_2 species in SEI for faster Ca^{2+} diffusion. Therefore, we propose the addition of anion receptors to raise CaI_2 solubility. Anion receptors,
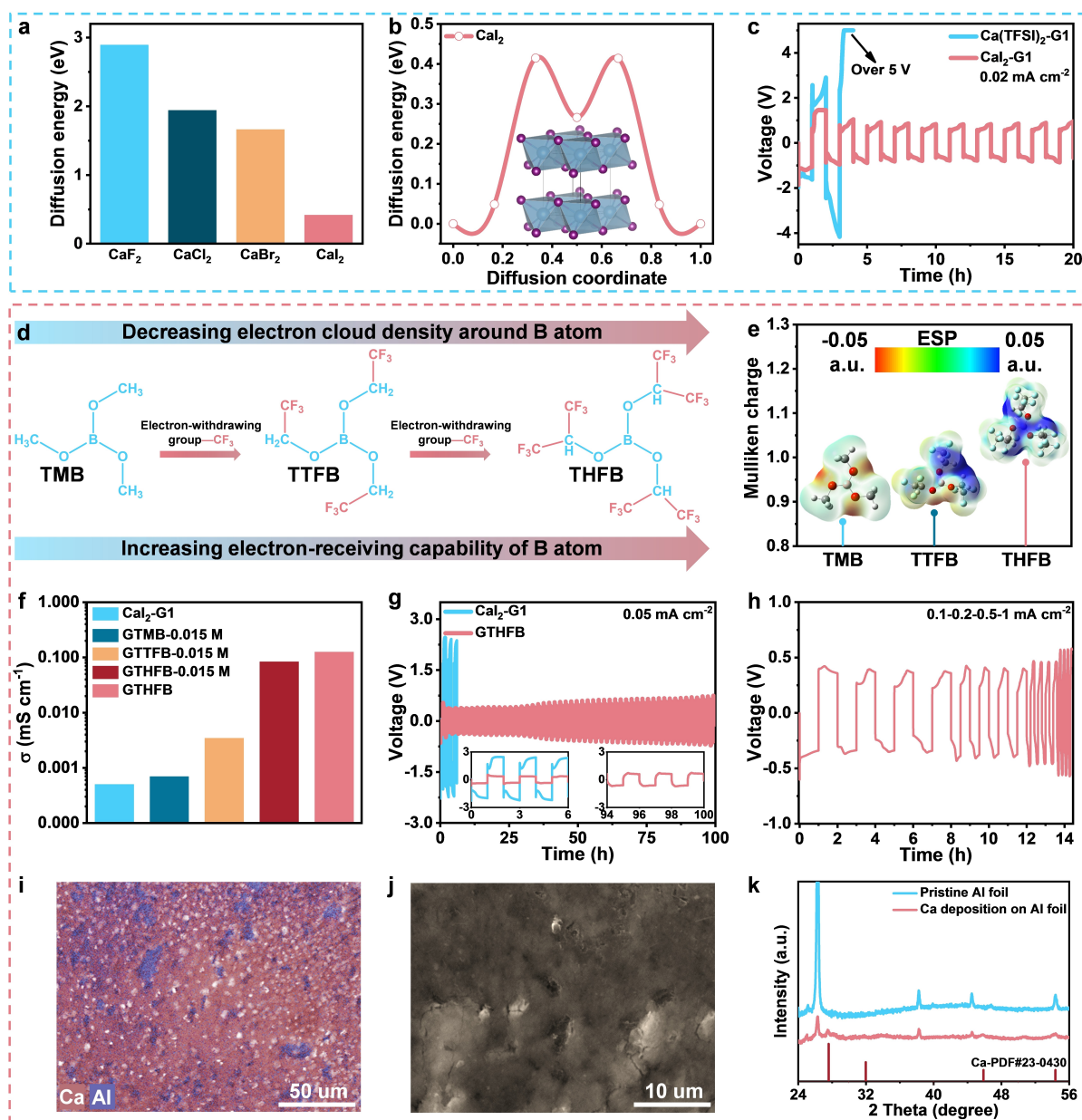
Figure 1. Screening inorganic Ca^{2+} conducting phases for Ca electrolyte development. a) Diffusion barriers in CaF_2, $CaCl_2$, $CaBr_2$ and CaI_2. b) Ca^{2+} diffusion energy landscape in CaI_2 and the inset is its layered structure. c) Cycling performance of Ca|Ca cells at 0.02 mA cm^{-2} in CaI_2-G1 and Ca(TFSI)$_2$-G1 electrolytes. d) The influences of $-CF_3$ group on B atoms' electron-receiving capability. e) ESP mappings and Mulliken charge of B atom in borate ester anion receptors. f) Bulk ionic conductivities (σ) of various electrolytes. g) Cycling performance of Ca|Ca cells at 0.05 mA cm^{-2} in CaI_2-G1 and GTHFB electrolytes. h) Rate capability of Ca|Ca cells in GTHFB electrolyte. i,j) EDS elemental mapping and SEM image of Ca deposition on carbon-coated Al current collector under 0.5 mAh cm^{-2} in GTHFB electrolyte. k) XRD patterns of carbon-coated Al current collector before and after 0.5 mAh cm^{-2} Ca deposition in GTHFB electrolyte.

possessing an electron-deficient center, can act as Lewis acid to strongly interact with Lewis based anions for facilitating salt dissociation.[17] There are many types of anion receptors, such as boron-, amide- and urea-based ones.[18] Owing to a low Ca/Ca^{2+} redox potential, anion receptors inevitably undergo electro-decomposition and participate in SEI formation. Thus, boron-based anion receptors should be a preferred choice since a few boron species (e.g., cross-linked boron polymer) have been reported to promote Ca^{2+} diffusion.[7]

We assess a serial of borate ester anion receptors with a formula B(OR)$_3$, including trimethyl borate (TMB), tris(2,2,2-trifluoroethyl) borate (TTFB) and tris(2H-hexa-fluoroisopropyl) borate (THFB) (Figure 1d). B atoms with an empty orbital are expected to combine with I$^-$, in turn facilitating CaI$_2$ dissociation and dissolution. We regulate the electron-receiving capability of the B center by gradually grafting electron-withdrawing $-CF_3$ group to the terminal R group of TMB. Electronic static potentials (ESP) of these anion receptors are calculated to examine the effects of

Angew. Chem. Int. Ed. **2025**, *64*, e202413416 (3 of 9)

© 2024 The Authors. Angewandte Chemie International Edition published by Wiley-VCH GmbH

–CF$_3$ group on electron cloud distribution (Figure 1e). It is observed that electron cloud density around B atom experiences a decrease with the addition of –CF$_3$ group, leading to a reduced electronegativity of B atom. It is worth noting that the B(OR)$_3$ structures seem to be of central symmetry from the chemical formula. But in reality, they are not. Especially for TTFB, the two CF$_3$ pointing up while one pointing down is the lowest energy configuration. This leads to the asymmetry of ESP mappings. Besides, THFB possesses the highest positive Mulliken charge on B atom than TMB and TTFB. These observations suggest that the introduction of electron-withdrawing –CF$_3$ group enhances electron-receiving ability of B atom, which is expected to facilitate CaI$_2$ dissociation. To verify it, the corresponding electrolytes are fabricated by dissolving the same concentration of CaI$_2$, i.e., 0.015 M, into a mixture of G1/TMB, G1/TTFB and G1/THFB (9:1 in weight and abbreviated as GTMB-0.015 M, GTTFB-0.015 M and GTHFB-0.015 M), and their bulk ionic conductivities are collected (Figure 1f and Figure S2). The introduction of –CF$_3$ group benefits CaI$_2$ dissociation, evidenced by an increased ionic conductivity from CaI$_2$-G1 (5.0×10^{-4} mS cm^{-1}) to GTMB-0.015 M (6.9×10^{-4} mS cm^{-1}), GTTFB-0.015 M (3.4×10^{-3} mS cm^{-1}) and GTHFB-0.015 M (0.08 mS cm^{-1}) electrolytes. The stronger electron-receiving capability of THFB is further confirmed by easily preparing GTHFB electrolyte with a higher concentration of 0.1 M CaI$_2$ in a mixture of G1/THFB (9:1 in weight), while G1/TMB and G1/TTFB solvents fail to dissolve 0.1 M CaI$_2$. Owing to a higher CaI$_2$ concentration, the GTHFB electrolyte owns a slightly larger ionic conductivity of 0.13 mS cm^{-1} than that of the GTHFB-0.015 M one.

Subsequently, we explore Ca reversibility in these five electrolytes by testing Ca|Ca cells and Ca|Al cells. As shown in Figure S5a, Ca|Ca cell delivers a large deposition/stripping overpotential of ~2.5 V in CaI$_2$-G1 electrolyte when a relatively high current density of 0.05 mA cm^{-2} is applied. This value decreases to ~1.3 V in GTMB-0.015 M electrolyte, followed by ~0.50 V in GTTFB-0.015 M and ~0.35 V in GTHFB-0.015 M, which agree with the order of their bulk ionic conductivities. The voltage polarization is further reduced in GTHFB electrolyte with higher ionic conductivity (Figure 1g), enabling a stable deposition/stripping lifetime over 100 h. A similar trend is also observed in galvanostatic Coulombic efficiency (CE) performance obtained from Ca|Al cells (Figure S5c). For example, after 20 cycles, GTHFB electrolyte exhibits a decent CE of ~71%, which is higher than ~63% and ~54% in GTHFB-0.015 M and GTTFB-0.015 M ones (Figure S5d). Besides, similar CE of ~70% is achieved from cyclic voltammetry (CV) tests of Ca|Al cells in GTHFB electrolyte (Figure S5e). Therefore, the optimal Ca reversibility is achieved in the GTHFB electrolyte system, which will be used as the model system to figure out the working mechanism of borate ester anion receptors.

To further examine the effectiveness of GTHFB electrolyte, Ca|Ca cells are also tested at 0.1 mA cm^{-2} for 2 h with reasonable stability (Figure S5b). Besides, the GTHFB electrolyte displays a decent rate capability, delivering a reversible Ca deposition/stripping at a high current density of 1 mA cm^{-2} (Figure 1h). Scanning electron microscope (SEM) images, the corresponding energy dispersive spectroscopy (EDS) elemental mappings and X-ray diffraction (XRD) patterns are also collected to inspect deposition products. As shown in Figure S6 and Figure 1i and j, Ca signals are well overlapped with deposits in EDS elemental mappings, indicating the Ca metal deposition that is also proved by XRD patterns (Figure 1k).

Optimized Solvation Sheath and SEI Structure in the Presence of Borate Ester Anion Receptors

Having known that the addition of THFB anion receptor can boost Ca deposition/stripping behavior, we next aim to unravel its working mechanism. EIS is performed using Ca|Ca cells in CaI$_2$-G1 and GTHFB electrolytes (Figure 2a and Figure S7). An equivalent circuit, including bulk resistance (R_b), charge transfer resistance (R_{ct}) and SEI resistance (R_{SEI}), is employed to analyze their Nyquist plots (Figure S3e). Figure 2b presents that R$_b$ value is reduced from ~10330 to ~38 Ω after adding THFB, proving an enhanced Ca^{2+} diffusion in bulk GTHFB electrolyte that is consistent with their ionic conductivity results. Besides, a slightly smaller R_{ct} of 2347 Ω is detected in GTHFB electrolyte compared to that in CaI$_2$-G1 one (12780 Ω). Note that R_{ct} primarily corresponds to Ca^{2+} desolvation barrier in this case.[19] Apart from the reduced R$_b$ and R_{ct}, we observe a significantly decreased R$_{SEI}$ from 3.3×10^5 Ω in CaI$_2$-G1 electrolyte to 3.8×10^4 Ω in GTHFB one, indicating an enhanced Ca^{2+} diffusion within GTHFB electrolyte' SEI.

Considering that both Ca^{2+} mass transfer and desolvation process are highly related to electrolytes' solvation structures, we employ Raman spectra, nuclear magnetic resonance (NMR) spectroscopy and theoretical calculations to understand the deceased R$_b$ and R_{ct} in GTHFB electrolyte. Raman spectra are carried out to assess interactions among THFB, G1 and CaI$_2$. As shown in Figure 2c, after adding G1 solvent into pure THFB, the bending vibration (δ) of BO$_3$ experiences a minor redshift, implying an increased bond length and decreased bond strength of the B–O bond.[20] This should be ascribed to a weak coordination between G1 molecules and BO$_3$ groups of THFB. We further add CaI$_2$ into the hybrid G1/THFB solvent, and observe a major redshift of δ(BO$_3$), indicating a strong interaction between I$^-$ and BO$_3$ groups. In addition, ^{11}B NMR spectra are carried out to further examine chemical environments of B center with/without CaI$_2$. In hybrid G1/THFB solvent, there are two peaks at ~17.4 ppm and ~1.6 ppm (Figure 2d). The former corresponds to THFB, i.e., tri-coordinated B[OCH(CF$_3$)$_2$]$_3$, while the latter is assigned to tetra-coordinated B[OCH(CF$_3$)$_2$]$_4^-$ according to the previous reports.[21] Their peak positions almost remain unchanged after adding CaI$_2$ salt. However, a new peak with a high intensity appears at ~1.1 ppm, which should be designated to (THFB·I)$^-$ anion, formed by Lewis acid-base reaction between THFB and I$^-$. These experimental observations are further confirmed by theoretical calculations.
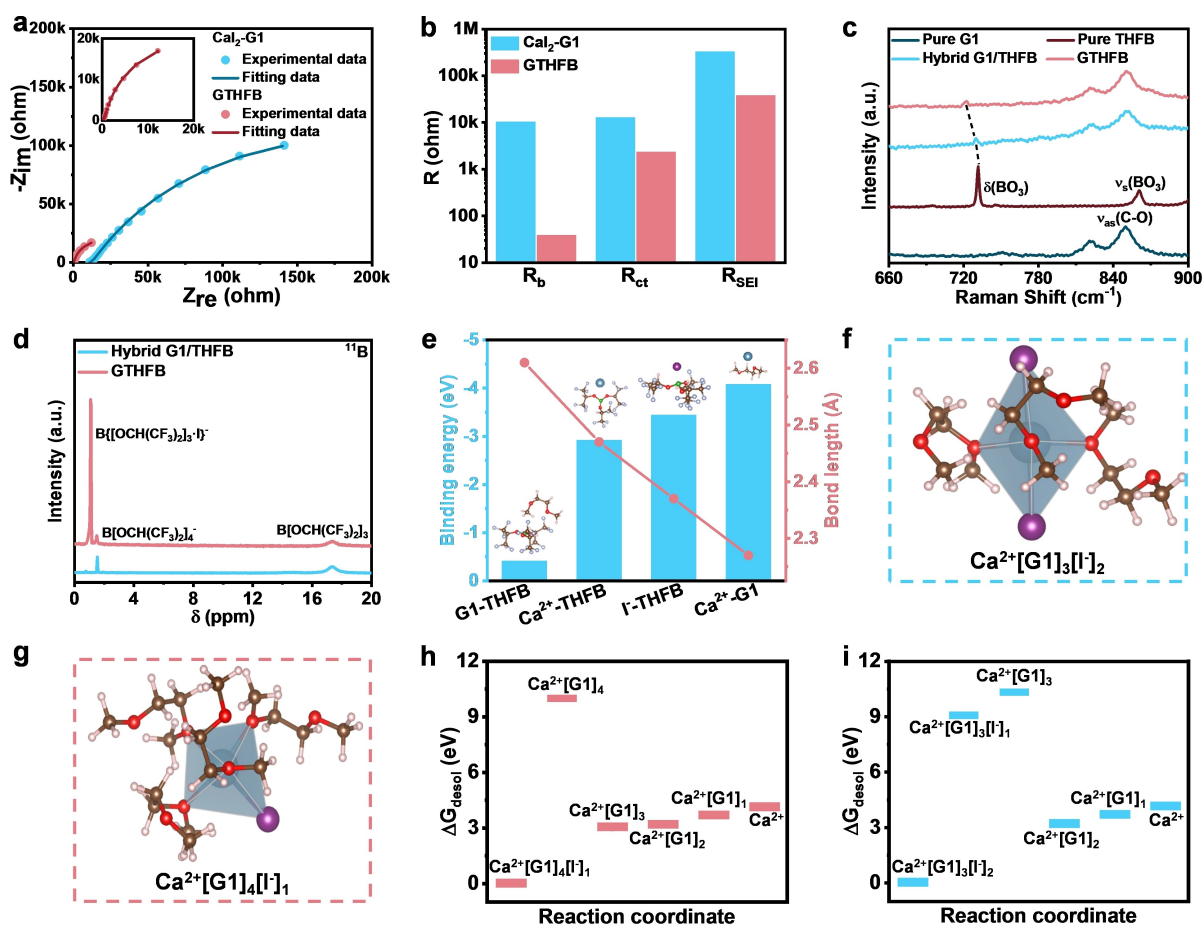
Figure 2. Characterization of solvation structures under CaI₂-G1 and GTHFB electrolytes. a) Experimental and fitting EIS Nyquist plots and b) the corresponding fitting results of Ca|Ca cells after 5 cycles. The inset in a) is the enlarged Nyquist plot of GTHFB electrolyte. c) Raman spectra of pure solvents, hybrid G1/THFB solvent (9:1 in weight) and electrolytes. d) NMR spectra of G1/THFB solvent and GTHFB electrolyte. e) Binding energies and bond lengths among cation, anion and solvents. Typical solvation structure of Ca²⁺ (1st sheath) in f) 0.2 M CaI₂ in G1 and g) 1 M CaI₂ in G1/THFB (9:1). The desolvation steps and energies of h) Ca²⁺[G1]₄[I⁻]₁ solvation structure in 1 M CaI₂ in G1/THFB and i) Ca²⁺[G1]₃[I⁻]₂ solvation structure in 0.2 M CaI₂ in G1.

THFB shows the highest binding energy with I⁻ than G1 and Ca²⁺, leading to the shortest bond length (Figure 2e). These results indicate the strongest interaction between THFB and I⁻ in the electrolyte, consistent with Raman and NMR results. Namely, THFB facilitates CaI₂ dissociation through strongly interacting with I⁻, resulting in a higher ionic conductivity and increased R_b.

Turning to desolvation process-related R_ct, molecular dynamics (MD) simulations are carried out to quantitatively analyze Ca²⁺ solvation structure in CaI₂-G1 and GTHFB electrolytes. As shown in Figure 2f and g and Figure S8, most Ca²⁺ are coordinated by ~3 G1 and ~2 I⁻ in CaI₂-G1 electrolyte, while THFB addition alters the solvation structure into Ca²⁺[G1]₄[I⁻]₁. This change can be ascribed to the strong interaction between THFB and I⁻, bringing about reduced I⁻ and increased G1 around Ca²⁺. The relative desolvation energy (ΔG_desol) of Ca²⁺[G1]₃[I⁻]₂ and Ca²⁺[G1]₄[I⁻]₁ solvation structures are subsequently calculated using DFT to understand the reduced R_ct in GTHFB electrolyte (Figure 2h and i). It is found that Ca²⁺[G1]₄[I⁻]₁ solvation structure presents a similar G_desol of I⁻ with that in

Ca²⁺[G1]₃[I⁻]₂ for the 1st step. By sharp contrast, during the 2nd step, a significantly smaller G_desol of G1 is observed in Ca²⁺[G1]₄[I⁻]₁ under the GTHFB electrolyte compared to G_desol of I⁻ in Ca²⁺[G1]₃[I⁻]₂ under CaI₂-G1 electrolyte, which is attributed to the stronger interaction between Ca²⁺ and I⁻ than G1. The following desolvation processes involve the transition from Ca²⁺[G1]₃ to Ca²⁺ in both solvation structures, leading to the same G_desol values. Consequently, the overall desolvation energy in GTHFB electrolyte is slightly lower than that in CaI₂-G1 electrolyte, consistent with the smaller R_ct.

It is worth noting that R_SEI accounts for a large proportion (over 90%) of total resistances in both electrolytes. Namely, Ca²⁺ transfer within the SEIs plays a key role in determining Ca reversibility. To reveal SEIs discrepancy in CaI₂-G1 and GTHFB electrolytes, we carry out depth-profiling X-ray photoelectron spectroscopy (XPS) and time-of-flight secondary ion mass spectrometry (TOF-SIMS). XPS results show that their SEIs share similar organic species originating from the same G1 solvent decomposition, as indicated by the C–C, C–O and C=O bonds in

© 2024 The Authors. Angewandte Chemie International Edition published by Wiley-VCH GmbH

deconvoluted C 1s and O 1s spectra (Figure 3a and b and Figure S9–S11). Besides, many inorganic species, including CaO, $CaCO_3$ and CaI_2, are detected in their SEIs. Noteworthily, CaI_2 species not only exist on the Ca metal anode's surface but are also present after Ar ion sputtering for 300 s, proving that it constitutes a part of SEIs. Considering that different CaI_2 concentrations in CaI_2-G1 and GTHFB electrolytes potentially influence the CaI_2 content in SEIs, we analyze their elemental ratios. It is observed that the GTHFB electrolyte with a higher concentration results in a slightly higher I content, indicating the increased CaI_2 species in its SEI that is beneficial to transferring Ca^{2+}. This is similar to the previous alkali metal anodes' studies where high-concentration electrolytes are preferred to induce the salt-derived SEIs.[22] Besides, the addition of THFB leads to

the alteration of C and O atomic ratios, which should be ascribed to the decomposition of THFB. To evaluate whether THFB participates in SEI formation process, we collect XPS spectra of B and F elements, which are absent in THFB-free electrolyte. As shown in Figure 3c and Figure S11j, the existence of B–O and Ca–F bonds confirms that THFB suffers from electro-reduction during cycling. Besides, the formation of B–O species is further observed in O 1s spectra. Note that boron-based components may help facilitate Ca^{2+} diffusion within SEI. These observations are also verified by TOF-SIMS measurement (Figure 3d). Specifically, organic C_2H_5 and C_2H_3O, mainly induced by G1 solvent, are detected in both electrolytes with a similar intensity. Turning to the CaI signal, it exists throughout the sputtering process. Its intensity is slightly higher in GTHFB
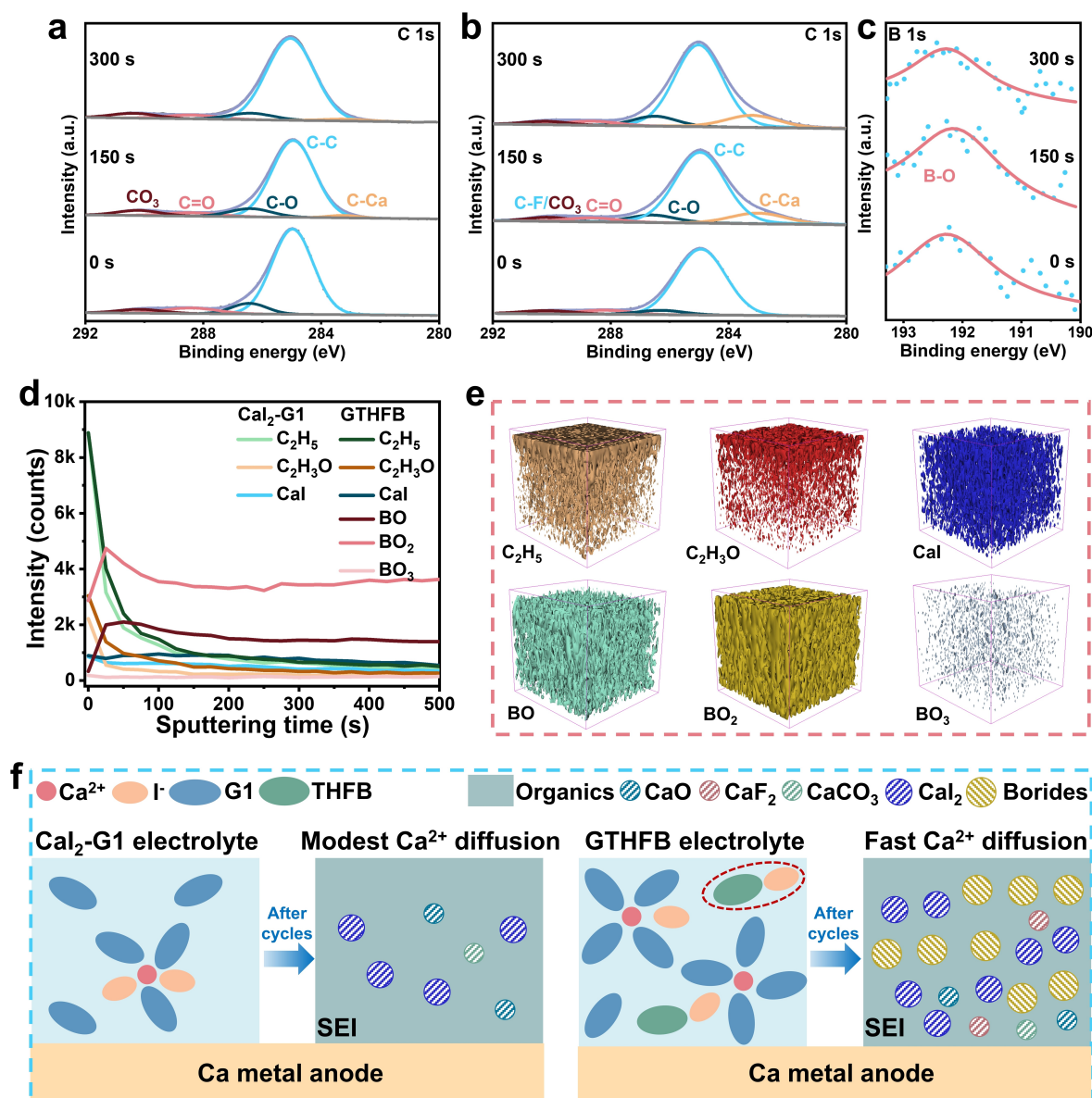

Figure 3. SEIs feature under CaI_2-G1 and GTHFB electrolytes. C 1s spectra of SEIs formed in a) CaI_2-G1 and b) GTHFB electrolytes. c) B 1s spectra of SEIs formed in GTHFB electrolyte. d) TOF-SIMS intensity evolution of SEI species as a function of sputtering time. e) TOF-SIMS 3D render images of SEI formed in GTHFB electrolyte. f) Illustration of working mechanism with THFB anion receptor.

electrolyte than that in CaI$_2$-G1 counterpart, which is also displayed in their 3D render images (Figure 3e and Figure S12), consistent with the XPS results. Besides, the signals of BO, BO$_2$ and BO$_3$ species are detected due to the decomposition of THFB. These results demonstrate that primary differences between SEIs derived from CaI$_2$-G1 and GTHFB electrolytes consist of an increased CaI$_2$ species and the formation of unique B–O compositions in the latter.

DFT calculations are performed to understand the electro-reduction process of THFB. Based on XPS and TOF-SIMS results, we propose its possible decomposition pathways and the corresponding dissociation energies (Figure S13), leading to the formation of many boron-based components, such as Ca(BO$_3$(CHC$_2$F$_6$)$_2$)$_2$, Ca(BO$_3$CHC$_2$F$_6$)$_2$, Ca[(BO$_2$)$_2$]$_n$, Ca$_3$(BO$_3$)$_2$. To reveal the effects of these species on Ca^{2+} diffusion within SEI, their diffusion barriers are simulated (Figure S14). It is found that these species show small diffusion barriers, especially for Ca(BO$_3$-(CHC$_2$F$_6$)$_2$)$_2$ (~0.57 eV), Ca(BO$_3$CHC$_2$F$_6$)$_2$ (~0.60 eV), and Ca((BO$_2$)$_2$)$_n$ (~0.75 eV). The values are only slightly higher than 0.4 eV for CaI$_2$ but much lower than that of CaF$_2$ and CaCO$_3$, implying these borides own a decent Ca^{2+} conductivity. Namely, apart from ionic conductive CaI$_2$, these borides are also responsible for conducting Ca^{2+} within SEIs, leading to a highly decreased R$_{SEI}$ in GTHFB electrolyte for reduced polarization (Figure S15).

Based on the above observations, we depict the working mechanism of THFB. As shown in Figure 3f, pristine CaI$_2$-G1 electrolyte suffers from a low CaI$_2$ concentration, leading to a low bulk ionic conductivity and modest Ca^{2+} diffusion within SEI. The addition of THFB anion receptor promotes CaI$_2$ dissociation through strongly interacting with I$^-$, leading to a higher CaI$_2$ concentration. This improves bulk ionic conductivity and induces more CaI$_2$ species in SEIs. Furthermore, THFB participates in the electro-reduction process, forming CaI$_2$/borides hybrid SEIs with a faster Ca^{2+} conductivity than individual CaI$_2$ phases in CaI$_2$-G1 electrolyte' SEI. Thanks to these synergistic effects, improved Ca/Ca^{2+} redox reaction kinetics is realized in GTHFB electrolyte.

Constructing Full Cells

Lastly, we assess the practical application of GTHFB electrolyte through assembling full cells with promising cathodes. Thanks to the decent electrochemical window of over 3.1 V (Figure S16a), GTHFB electrolyte is compatible with organic PTCDI cathode, enabling stable Ca-PTCDI full cells for over 100 cycles (Figure 4a). The slightly declined capacity of Ca-PTCDI full cells is ascribed to the PTCDI dissolution in the electrolyte, as evidenced by the optical images of the separator in cycled cells (Figure S17). Besides, Ca-PTCDI full cells show an attractive rate capability where specific capacity is slightly decreased from ~60 mAh g^{-1} in 0.1 A g^{-1} to ~51 mAh g^{-1} in 0.5 A g^{-1} (Figure 4b). EDS mappings of discharged and charged PTCDI cathodes display a reversible Ca combination/release process during cycling (Figure S18). Moreover, an inorganic Se cathode
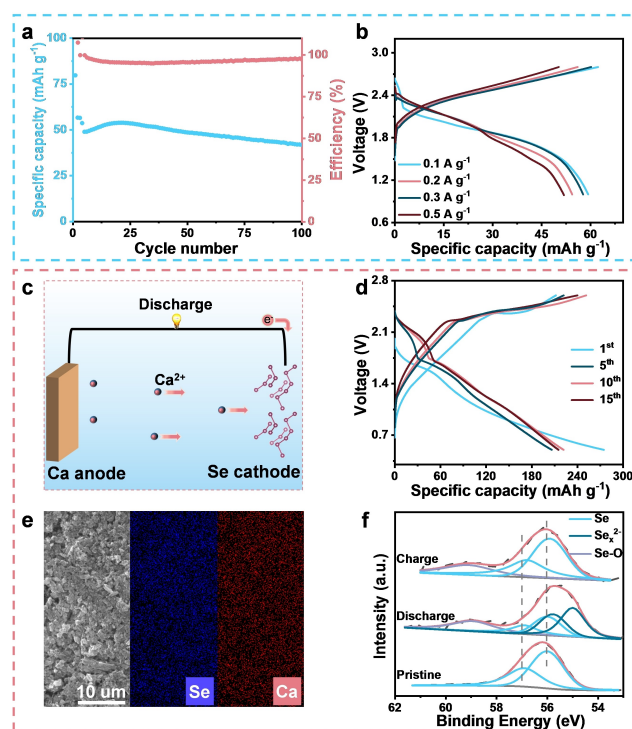

Figure 4. Ca-PTCDI and Ca–Se full cells in GTHFB electrolyte. a) Cyclic stability of Ca-PTCDI full cell at 300 mA g^{-1}. b) Rate performance of Ca-PTCDI full cell. c) Schematic of Ca–Se full cell during the discharge process. d) Detailed discharged/charged curves of Ca–Se full cell. e) SEM image and the corresponding EDS elemental mappings of discharged Se cathode. f) Se 3d spectra at different electrochemical states.

with a high capacity is tested in GTHFB electrolyte. As shown in Figure 4c and Figure S16b, reversible Ca–Se full cell can be achieved. However, it suffers from a rapid capacity decay, probably due to the fact that the intermediate discharged product polyselenides are easily dissolved in electrolytes.[23] To restrain the shuttle of dissolved polyselenides, a free-standing reduced graphene oxide/carbon nanotube interlayer is introduced between the Se cathode and separator. Delightfully, Ca–Se batteries with an interlayer can stably run for 15 cycles, delivering a high capacity of ~200 mAh g^{-1} (Figure 4d and Figure S16c). Similarly, EDS mappings prove a reversible conversion reaction between Ca and Se (Figure 4e and Figure S19). This is further confirmed by Se 3d XPS results where signals of pristine Se move to lower binding energies after discharge (Figure 4f), which is assigned to polyselenides CaSe$_x$ ($x > 1$). Upon charging, the peaks return to the position of pristine Se, indicating the reversible transition of CaSe$_x$ to Se. Note that the Se–O bond is formed during the discharge/charge process, which may be ascribed to the reaction between Se anions with electrolytes.[24] These observations demonstrate the potential applications of GTHFB electrolyte.

Conclusion

This work proposes a novel CaI_2-G1 electrolytes for reversible Ca metal anodes, adding another dimension to Ca electrolyte chemistry. Complementary theoretical and experimental investigations demonstrate that CaI_2-based electrolytes' uniqueness is attributed to the formation of SEI consisting of the ionic-conductive CaI_2 species, which shows an extremely low Ca^{2+} migration barrier. This is the first reported inorganic phase showing promising Ca^{2+} diffusivity, thus providing opportunities to design highly ionic conductive interfaces in future studies. In addition, we further boost the deposition/stripping reaction kinetics by introducing a collection of borate ester anion receptors with a formula $B(OR)_3$ where B atoms' electron cloud density can be controlled by gradually grafting electron-withdrawing $-CF_3$ group to terminal R group. In particular, the THFB anion receptor with the highest fluorination degree possesses the strongest electron-receiving capability and shows optimal merits. Firstly, its electron-deficient B center as Lewis acid can dramatically interact with I^-, promoting CaI_2 salt dissociation and dissolution. This benefits an increased CaI_2 solubility from ~0.015 to 0.1 M, achieving 200-fold enhancement in bulk ionic conductivity. Furthermore, THFB anion receptor experiences electro-decomposition during cycling, leading to the formation of CaI_2/borides hybrid SEI for rapid Ca^{2+} diffusion. Thanks to these synergetic effects, Ca deposition/stripping polarization is reduced from ~2.5 to ~0.35 V in the presence of THFB. Furthermore, Ca-PTCDI and Ca–Se full cells display a stable operation in THFB-containing electrolyte.

The exciting results reported here extend the knowledge in the field of Ca electrolyte chemistry, yet they do not fully meet the requirements of Ca metal batteries' practical applications, leaving ample scope for improvement. On the one hand, fluorinated THFB inevitably leads to passivating CaF_2 species present in SEIs, which is detrimental to the long-term stability of Ca metal anodes. Besides, commercially available THFB exhibits sensitivity to moisture environments, limiting its practical applicability in Ca electrolyte. Future research necessitates the exploitation of more robust anion receptor candidates to promote CaI_2 dissociation without introducing detrimental SEI species. On the other hand, I^- anions result in a slightly low oxidation voltage, limiting the utilization of many high-voltage cathodes. Exploring alternative iodine salts with a higher valence state, such as calcium iodate $Ca(IO_3)_2$, holds promise for stabilizing iodine-based electrolytes and facilitating the development of high-voltage Ca systems. We hope that our findings will stimulate further advancements in the field of Ca metal-based electrolyte chemistry and battery technology.

Supporting Information

The authors have cited additional references within the Supporting Information.

Conflict of Interest

The authors declare no conflict of interest.

Data Availability Statement

The data that support the findings of this study are available from the corresponding author upon reasonable request.

[1] a) Y. Liang, H. Dong, D. Aurbach, Y. Yao, *Nat. Energy* **2020**, *5*, 646–656; b) W. Zhao, Z. Pan, Y. Zhang, Y. Liu, H. Dou, Y. Shi, Z. Zuo, B. Zhang, J. Chen, X. Zhao, *Angew. Chem. Int. Ed.* **2022**, *61*, e202205187; c) S. Hou, X. Ji, K. Gaskell, P.-F. Wang, L. Wang, J. Xu, R. Sun, O. Borodin, C. Wang, *Science* **2021**, *374*, 172–178; d) H. Zhang, L. Qiao, H. Kühnle, E. Figgemeier, M. Armand, G. G. Eshetu, *Energy Environ. Sci.* **2023**, *16*, 11–52; e) Y. Liu, W. Zhao, Z. Pan, Z. Fan, M. Zhang, X. Zhao, J. Chen, X. Yang, *Angew. Chem. Int. Ed.* **2023**, *135*, e202302617; f) Z. Zhang, M. Song, C. Si, W. Cui, Y. Wang, *eScience* **2023**, *3*, 100070.

[2] a) R. J. Gummow, G. Vamvounis, M. B. Kannan, Y. He, *Adv. Mater.* **2018**, *30*, e1801702; b) M. E. Arroyo de Dompablo, A. Ponrouch, P. Johansson, M. R. Palacin, *Chem. Rev.* **2020**, *120*, 6331–6357; c) I. D. Hosein, *ACS Energy Lett.* **2021**, *6*, 1560–1565; d) Q. Wei, L. Zhang, X. Sun, T. L. Liu, *Chem. Sci.* **2022**, *13*, 5797–5812; e) Z. Zhao-Karger, Y. Xiu, Z. Li, A. Reupert, T. Smok, M. Fichtner, *Nat. Commun.* **2022**, *13*, 3849; f) M. Wang, C. Jiang, S. Zhang, X. Song, Y. Tang, H. M. Cheng, *Nat. Chem.* **2018**, *10*, 667–672; g) Z. Hou, R. Zhou, Z. Min, Z. Lu, B. Zhang, *ACS Energy Lett.* **2022**, *8*, 274–279; h) T. Masese, G. M. Kanyolo, *EcoEnergy* **2024**, https://doi.org/10.1002/ece2.53.

[3] a) S. Biria, S. Pathreeker, H. Li, I. D. Hosein, *ACS Appl. Energ. Mater.* **2019**, *2*, 7738–7743; b) H. Song, J. Su, C. Wang, *Adv. Mater.* **2021**, *33*, e2006141; c) N. T. Hahn, J. Self, T. J. Seguin, D. M. Driscoll, M. A. Rodriguez, M. Balasubramanian, K. A. Persson, K. R. Zavadil, *J. Mater. Chem. A* **2020**, *8*, 7235–7244; d) K. Ta, R. Zhang, M. Shin, R. T. Rooney, E. K. Neumann, A. A. Gewirth, *ACS Appl. Mater. Interfaces* **2019**, *11*, 21536–21542; e) S. A. McClary, D. M. Long, A. Sanz-Matias, P. G. Kotula, D. Prendergast, K. L. Jungjohann, K. R. Zavadil, *ACS Energy Lett.* **2022**, *7*, 2792–2800; f) A. M. Melemed, A. Khurram, B. M. Gallant, *Batter Supercaps* **2020**, *3*, 570–580.

[4] D. Aurbach, R. Skaletsky, Y. Gofer, *J. Electrochem. Soc.* **1991**, *138*, 3536.

[5] a) N. T. Hahn, S. A. McClary, A. T. Landers, K. R. Zavadil, *J. Phys. Chem. C* **2022**, *126*, 10335–10345; b) D. M. Driscoll, N. K. Dandu, N. T. Hahn, T. J. Seguin, K. A. Persson, K. R. Zavadil, L. A. Curtiss, M. Balasubramanian, *J. Electrochem. Soc.* **2020**,

167, 160512; c) Z. Yu, P. E. Rudnicki, Z. Zhang, Z. Huang, H. Celik, S. T. Oyakhire, Y. Chen, X. Kong, S. C. Kim, X. Xiao, H. Wang, Y. Zheng, G. A. Kamat, M. S. Kim, S. F. Bent, J. Qin, Y. Cui, Z. Bao, *Nat. Energy* **2022**, *7*, 94–106; d) Z. Hou, R. Zhou, Y. Yao, Z. Min, Z. Lu, Y. Zhu, J. M. Tarascon, B. Zhang, *Angew. Chem. Int. Ed.* **2022**, *61*, e202214796.

[6] A. Ponrouch, C. Frontera, F. Barde, M. R. Palacin, *Nat. Mater.* **2016**, *15*, 169–172.

[7] J. Forero-Saboya, C. Davoisne, R. Dedryvère, I. Yousef, P. Canepa, A. Ponrouch, *Energy Environ. Sci.* **2020**, *13*, 3423–3431.

[8] D. Wang, X. Gao, Y. Chen, L. Jin, C. Kuss, P. G. Bruce, *Nat. Mater.* **2018**, *17*, 16–20.

[9] a) X. Gao, X. Liu, A. Mariani, G. A. Elia, M. Lechner, C. Streb, S. Passerini, *Energy Environ. Sci.* **2020**, *13*, 2559–2569; b) Y. Jie, Y. Tan, L. Li, Y. Han, S. Xu, Z. Zhao, R. Cao, X. Ren, F. Huang, Z. Lei, *Angew. Chem. Int. Ed.* **2020**, *59*, 12689–12693.

[10] a) Z. Li, O. Fuhr, M. Fichtner, Z. Zhao-Karger, *Energy Environ. Sci.* **2019**, *12*, 3496–3501; b) A. Shyamsunder, L. E. Blanc, A. Assoud, L. F. Nazar, *ACS Energy Lett.* **2019**, *4*, 2271–2276; c) K. Kisu, S. Kim, T. Shinohara, K. Zhao, A. Zuttel, S. I. Orimo, *Sci. Rep.* **2021**, *11*, 7563; d) S. Li, J. Zhang, S. Zhang, Q. Liu, H. Cheng, L. Fan, W. Zhang, X. Wang, Q. Wu, Y. Lu, *Nat. Energy* **2024**, *9*, 285–297.

[11] N. J. Leon, S. Ilic, X. Xie, H. Jeong, Z. Yang, B. Wang, E. W. C. Spotte-Smith, C. Stern, N. Hahn, K. Zavadil, *J. Phys. Chem. Lett.* **2024**, *15*, 5096–5102.

[12] N. J. Leon, X. Xie, M. Yang, D. M. Driscoll, J. G. Connell, S. Kim, T. Seguin, J. T. Vaughey, M. Balasubramanian, K. A. Persson, C. Liao, *J. Phys. Chem. C* **2022**, *126*, 13579–13584.

[13] a) R. Attias, M. Salama, B. Hirsch, Y. Goffer, D. Aurbach, *Joule* **2019**, *3*, 27–52; b) J. Muldoon, C. B. Bucur, T. Gregory, *Chem. Rev.* **2014**, *114*, 11683–11720.

[14] P. Jankowski, W. Wieczorek, P. Johansson, *Phys. Chem. Chem. Phys.* **2016**, *18*, 16274–16280.

[15] a) R. Schwarz, M. Pejic, P. Fischer, M. Marinaro, L. Jörissen, M. Wachtler, *Angew. Chem. Int. Ed.* **2016**, *128*, 15182–15186; b) I. Shterenberg, M. Salama, Y. Gofer, E. Levi, D. Aurbach, *MRS Bull.* **2014**, *39*, 453–460.

[16] a) Y. Lu, Z. Tu, J. Shu, L. A. Archer, *J. Power Sources* **2015**, *279*, 413–418; b) J. Xiao, X. Zhang, H. Fan, Y. Zhao, Y. Su, H. Liu, X. Li, Y. Su, H. Yuan, T. Pan, Q. Lin, L. Pan, Y. Zhang, *Adv. Mater.* **2022**, *34*, e2203783; c) D.-T. Nguyen, A. Y. S. Eng, M.-F. Ng, V. Kumar, Z. Sofer, A. D. Handoko, G. S. Subramanian, Z. W. Seh, *Cell Rep. Phys. Sci.* **2020**, *1*, 100265.

[17] V. P. Reddy, M. Blanco, R. Bugga, *J. Power Sources* **2014**, *247*, 813–820.

[18] P. A. Gale, E. N. Howe, X. Wu, *Chem* **2016**, *1*, 351–422.

[19] Y. X. Yao, X. Chen, N. Yao, J. H. Gao, G. Xu, J. F. Ding, C. L. Song, W. L. Cai, C. Yan, Q. Zhang, *Angew. Chem. Int. Ed.* **2023**, *62*, e202214828.

[20] R. Chen, L. Zhu, F. Wu, L. Li, R. Zhang, S. Chen, *J. Power Sources* **2014**, *245*, 730–738.

[21] P. Jankowski, Z. Li, Z. Zhao-Karger, T. Diemant, M. Fichtner, T. Vegge, J. M. G. Lastra, *Energy Storage Mater.* **2022**, *45*, 1133–1143.

[22] Y. Yamada, J. Wang, S. Ko, E. Watanabe, A. Yamada, *Nat. Energy* **2019**, *4*, 269–280.

[23] R. Zhou, Z. Hou, Q. Liu, X. Du, J. Huang, B. Zhang, *Adv. Funct. Mater.* **2022**, *32*, 2200929.

[24] Y. Cui, A. Abouimrane, J. Lu, T. Bolin, Y. Ren, W. Weng, C. Sun, V. A. Maroni, S. M. Heald, K. Amine, *J. Am. Chem. Soc.* **2013**, *135*, 8047–8056.